Contents

Chapter 4

Photon source

A horizontal plan view of the photon beam line is shown in Fig. 4.1 with the major components labeled. The electron beam enters the figure from below ground at the left and is bent into the horizontal plane to enter the tagger building. There it passes through a pair of steering dipoles and passes through the bremsstrahlung radiator. Immediately downstream from from the radiator, the electron beam enters into the tagging spectrometer, where the primary beam is bent in the direction of the electron beam dump. The radiator crystal is thin enough that the average energy loss by the electrons in traversing the radiator is less than the intrinsic energy spread of the incident beam. Those electrons which lose a significant fraction of their initial energy inside the radiator predominantly do so by emitting a single bremsstrahlung photon. These degraded electrons are bent out of the primary beam inside the tagger magnet and exit the vacuum chamber through a thin window, passing through air for a short distance before they reach the tagging counters located near the focal plane of the spectrometer. The primary electron beam is contained inside vacuum all the way to the dump.

The photons that are produced in the radiator pass through a small hole bored in the return yoke of the tagger magnet in the forward direction. They then pass into an evacuated photon beam pipe and travel to the experimental hall. Just before entering Hall D, the photon beam passes through a small collimator which blocks a large fraction of the incident beam intensity, and selectively passes the coherent bremsstrahlung component. The primary collimator is housed in a separate enclosure from the experimental hall for shielding purposes. Debris from interactions along the inside surface of the collimator bore forms a halo around the photon beam that exits the primary collimator. The charged component of the halo is deflected away from the beam axis by a dipole "sweeping" magnet just downstream of the collimator and stopped

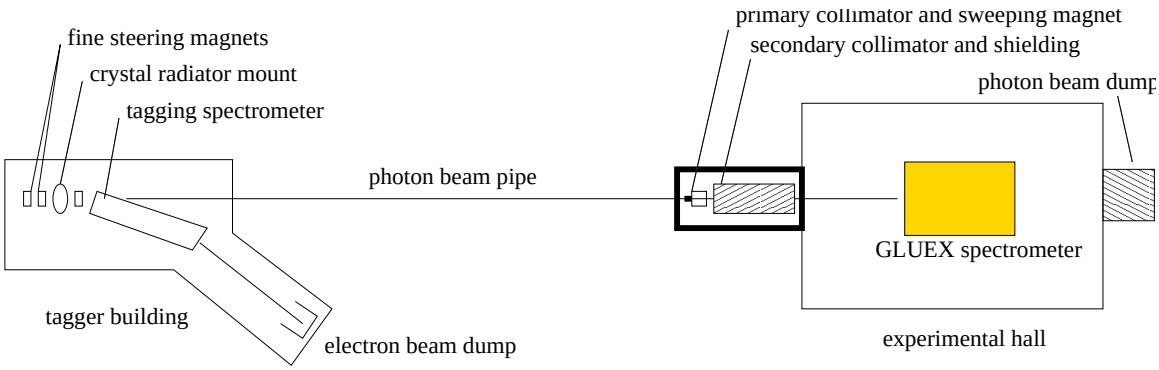

Figure 4.1: Schematic plan view of the photon beam line, shown in the horizontal plane as viewed from above. The objects in this figure are not drawn to scale.

in a thick wall of shielding material. Downstream of this there is a second collimator whose purpose is to block the halo of secondary photons generated by the first collimator. The secondary collimator is of a larger diameter than the primary and so sees a reduced rate of secondary interactions on the inner surface of the hole. What new showers are generated there are cleaned up by a second sweeping magnet. This two-stage collimation system is similar to the setup at the SLAC coherent bremsstrahlung beam line [1]. The clean collimated beam is then sampled in a pair spectrometer, which monitors the spectrum and flux of the beam just before it enters the experimental target.

After passing through of order 3% radiation lengths of liquid hydrogen in the GlueX target, the photon beam passes through the detector and into the photon beam dump at the back of the hall. Based upon a design upper limit of 60 kW (5 μA at 12 GeV) being delivered to the electron beam dump, the total power in the photon beam is not more than 1.5 W in the experimental hall and not more than 15 W in the collimator enclosure.

4.1 Essential features

The adjective 'coherent' in coherent bremsstrahlung does not indicate that the photons in the beam are in a coherent state, as is light from a laser. Rather it refers to the coherent effect of multiple atoms in a crystal lattice in absorbing the recoil momentum from a high energy electron when it radiates a bremsstrahlung photon. In X-ray spectroscopy one encounters the same thing in the Mössbauer effect. In that case, the chief physical consequence is the

disappearance of the recoil Doppler shift from the photoabsorption/emission spectrum. In the case of coherent bremsstrahlung, the chief consequence is the enhancement of the cross section at those particular kinematics for which the recoil momentum matches one of the reciprocal lattice vectors of the crystal.

It is helpful to view the process of coherent bremsstrahlung as virtual Compton scattering. To the high energy electron, the atoms in the radiator appear as clouds of virtual photons. For a disordered radiator material, the virtual photon spectrum is given simply by the atomic form factor, averaged over the different species in the material. If the radiator is a single crystal, however, the atomic form factor gets multiplied by the form factor of the crystal, which for an infinite static crystal looks like a series of delta-functions located at the sites of the reciprocal lattice. In effect, the crystal provides a set of virtual laser beams, each one a standing wave tuned to a specific reciprocal lattice vector. In this view, the process of hard bremsstrahlung is seen to be the same as Compton back-scattering of laser light. For a more detailed discussion of the physics of coherent bremsstrahlung there are a number of good references [1, 2, 3, 4].

The use of Compton back-scattering of laser light as a photon source was earlier noted as ruled out by the limitations of high-power laser cavities to wavelengths above 100 nm. The characteristic wavelength of the virtual photons in a crystal is a few Angstroms, three orders of magnitude shorter than the limit for lasers. At keV energies, 180° Compton scattering results in essentially 100% of the electron beam momentum being transferred to the photon in the lab frame. However, the Compton cross section contains a factor of $1/(\vec{q}\cdot\vec{p})^2$ where $\vec{q}$ is the virtual photon momentum and $\vec{p}$ is that of the electron. This factor strongly favors incident photons with $\vec{q}$ nearly orthogonal to $\vec{p}$. With reciprocal lattice vectors pointing in almost every direction, only those nearly perpendicular to the beam contribute appreciably to the scattering rate. This fact applies equally to ordinary bremsstrahlung; in fact, to a first approximation the bremsstrahlung spectrum from a single crystal is the same as that from a disordered radiator. The reason is that replacing the sum over crystal momenta in the coherent bremsstrahlung cross section formula with a continuous integral recovers the cross section for ordinary bremsstrahlung from isolated atoms.

Furthermore, beyond a few unit cells from the origin in reciprocal lattice space the atomic form factor and kinematic factors become slowly varying on the scale of the lattice spacing, so that the higher-order terms in the sum become indistinguishable from the the high-q part of the corresponding integral. Besides that, the uncertainty principle requires that atoms localized at the sites in a crystal undergo fluctuations about their mean position. This

has the effect of attenuating the discrete peaks in the crystal form factor at progressively higher-order crystal momenta, eventually washing them out and filling in the gaps between them, so that the sum deforms smoothly into the integral at high momentum transfer. Hence, the sum over crystal indices that yields the final photon spectrum can be separated into two parts: a discrete sum over a limited set of small crystal indices and an integral over the continuum of momentum transfer values beyond. The latter appears in the coherent bremsstrahlung beam as the ordinary continuum bremsstrahlung spectrum, while the former appears as a set of intensity peaks superimposed upon it. The $1/k$ continuum, referred to as the incoherent component, is invariant as the crystal is rotated, whereas the coherent peaks change in position and intensity, depending on crystal orientation.

A typical coherent bremsstrahlung spectrum is shown in Fig. 4.2. The distinction between incoherent and coherent components in the figure is artificial; it is there to distinguish the invariant part of the spectrum from the part that shifts as the crystal is rotated. The vertical scale in the figure gives the photon rate for the given beam current and crystal thickness. Note that the intensity of the incoherent background is less than what would be obtained with an amorphous carbon radiator of the same thickness, because a part of the momentum transfer integral in the Bethe-Heitler formula has been moved into the discrete sum and appears as the coherent part[1]. In the calculation used to produce Fig. 4.2, the leading 400 lattice sites were included in the discrete part of the calculation, but only two or three of them contribute with sufficient intensity to be identified with individual peaks visible in the spectrum.

4.2 Use of collimation

The presence of the large incoherent continuum in Fig. 4.2 presents a significant handicap to a photoproduction experiment. Not only do the continuum photons produce background in the detector, but they diminish the polarization of the beam. The entire beam polarization appears in the coherent component; the underlying incoherent flux only serves to dilute the polarization. However there is a difference between the angular distributions of the two components that allows them to be separated to some extent. The kinematics of bremsstrahlung confines most of the intensity of the photon beam to

[1]The typical figure of 12 cm for the radiation length of diamond is actually an average over all orientations of the crystal.

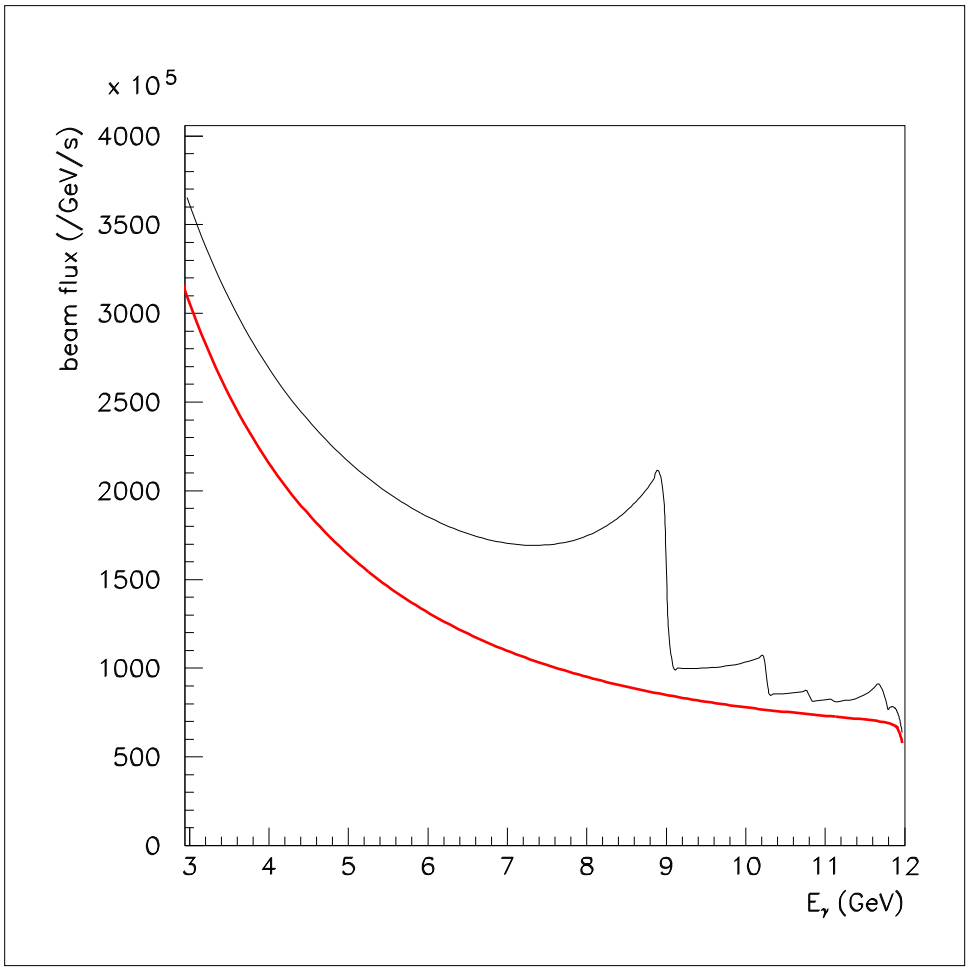

Figure 4.2: Uncollimated coherent bremsstrahlung spectrum, calculated for a diamond crystal radiator 20 microns thick and a 1 μA electron beam of 12 GeV energy. The sharpness of the edge at 9 GeV is a result of the excellent emittance of the 12 GeV electron beam.

forward angles within m/E radians of the incident electron direction[2]. This is true both for the incoherent and coherent components. The difference lies in the fact that a peak in the coherent component corresponding to a single reciprocal lattice vector has the two-body kinematics of Compton scattering, so there is a well-defined relation between the emission angle and the energy of the emitted photon in the lab: for a given reciprocal lattice vector, emission at 0° yields a maximum photon energy, and energy decreases with increasing angle. This accounts for the shape of the coherent peaks in Fig. 4.2, with the sharp right-hand edge of the peaks corresponding to 0° emission and the tail to lower energies corresponding to emission at higher angles.

The incoherent component, because it comes from a sum over momentum transfers at all angles, has essentially no correlation between photon energy and emission angle. This means that collimating away all photons beyond some angle $\theta_{max} < m/E$ uniformly attenuates the incoherent spectrum at all energies, whereas it preserves all of the coherent photons from the maximum energy for the given peak down to some cutoff. The kinematic relations for coherent bremsstrahlung are as follows,

$$\theta^2 + 1 = \left(\frac{1-x}{x}\right)\left(\frac{x_{max}}{1-x_{max}}\right) \tag{4.1}$$

$$x_{max} = \frac{2\vec{p}\cdot\vec{q}}{2\vec{p}\cdot\vec{q} - m_e^2} \tag{4.2}$$

where x is the photon energy in units of the incident electron energy and θ is the lab emission angle of the photon relative to the incident electron momentum axis, in units of m/E.

The effects of collimation are demonstrated in the calculated spectra shown in Fig. 4.3. First, note that the collimation angles are very small, which requires a long flight path of order 100 m in order that the collimator can be larger than the intrinsic beam spot size, otherwise the collimator is cutting in transverse coordinate instead of in angle. This distance is, in fact, a sensitive function of the electron beam emittance from the machine, and must be increased in proportion to the beam emittance if the effectiveness of collimation is held constant. This issue, along with the associated demands placed on beam alignment and position stability, are taken up in more detail in the following section on the electron beam line.

Second, note that the cut imposed on the coherent peak by collimation does not produce a perfectly sharp edge as would be expected from two-body

[2]In the lab frame this is a small angle, but in the rest frame of the electron-photon system it subtends all angles in the forward hemisphere.

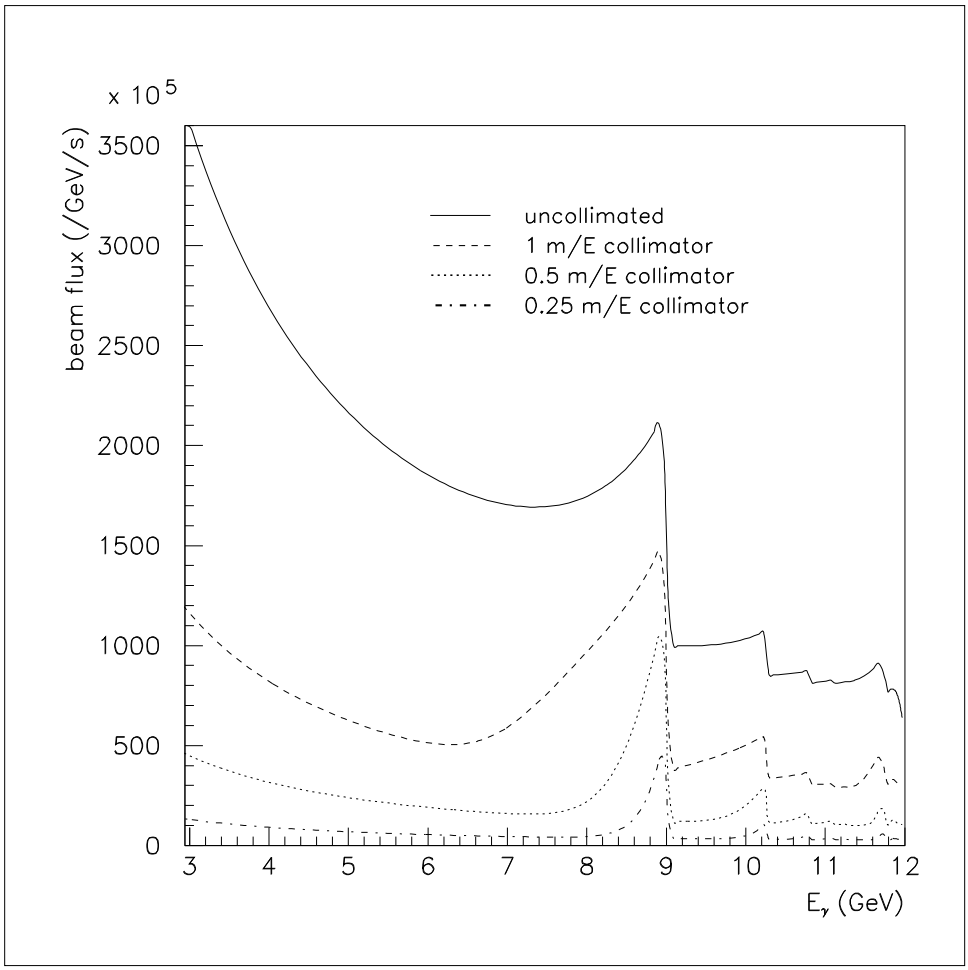

Figure 4.3: Coherent bremsstrahlung spectrum, calculated under the same conditions as in Fig. 4.2, with varying amounts of photon beam collimation. Curves shown from top to bottom are (1) the uncollimated spectrum, and collimated spectra with (2) a 1 m/E collimator, (3) a 0.5 m/E collimator, and (4) a 0.25 m/E collimator.

kinematics. This is because the collimator cuts on radius at some fixed distance, which translates into a cut on emission angle only in an approximate way. Multiple scattering by the electron in the radiator prior to emission, and beam spot size and divergence are the major contributors to the error involved in translating a collimator radius into a cut on emission angle. All of these effects have been incorporated into the analytical calculation of the yields from a collimated coherent bremsstrahlung source that has been used in optimizing the design of the source. Crystal imperfections, which amount to an intrinsic spread in the direction of the incoming virtual photon, are also taken into account in the model.

Third, note that the relatively weak collimation of 1 m/E reduces the incoherent background without significantly affecting the coherent flux near the maximum, thereby almost doubling the polarization of the beam at the peak relative to the uncollimated case. Further reducing the collimator diameter continues to narrow the peak and reduce the incoherent flux relative to the peak, albeit at some cost in peak intensity. The 0.5 m/E collimator has been chosen for this design because it provides for a maximum reduction in the incoherent flux while transmitting more than 90% of the coherent flux at the peak. This is implemented by placing a tungsten collimator with a circular aperture of diameter 3.4 mm at a distance 75 m downstream from the cyrstal.

Most of the photon beam energy coming from the crystal is absorbed by the collimator. To prevent the radiation produced at the collimator from producing background in the experimental, it is located in a separate enclosure just upstream of the experimental hall, and surrounded by a large amount of shielding. The peak in Fig. 4.3 for the 0.5 m/E collimator contains 4.8×10^7 photons/s in the primary coherent peak per μA of electron beam current. The GlueX experiment is designed to run at up to 10^8 photons/s in the coherent peak region 8.4-9.0 GeV. If the crystal is large enough to contain the entire electron beam spot at the radiator, this corresponds to 2.1 μA of electron beam current, safely below the design limit of 5 μA for the Hall D beam dump.

Fourth, note that the rate seen in the focal plane of the tagging spectrometer corresponds to the upper curve in Fig. 4.3, regardless of the collimation. This means that collimating the bremsstrahlung beam increases the rate in the tagger focal plane relative to what is seen at the detector. For full-intensity running at 10^8 photons/s on target in the coherent peak, Fig. 4.3 implies a rate of 250 MHz in the focal plane within a 600 MeV window around the peak. Combining this rate with the beam pulse spacing of 2 ns leads to an accidental tagging rate of about 50% and to a fraction of ambiguous tags of 40%. Even with ideal electronics, the per-second yield of single-tag events is close to saturation at this intensity. The detector and tagging spectrometer design

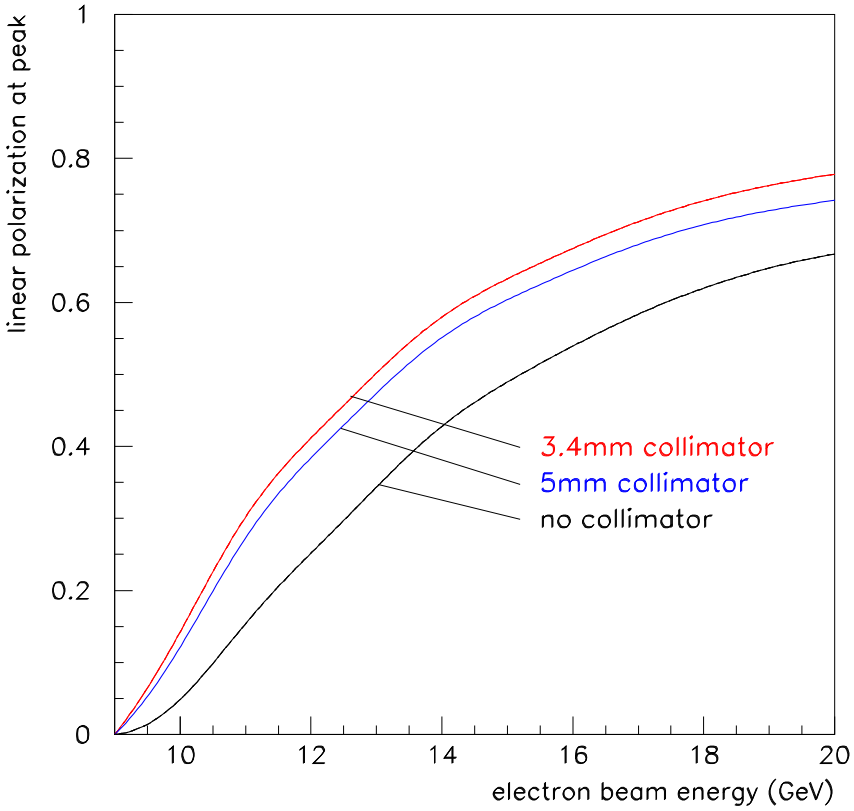

Figure 4.4: Linear polarization in the coherent bremsstrahlung peak as a function of electron beam energy keeping the energy of the coherent peak fixed at 9 MeV. The 3.4 mm [5 mm] collimator represents a cut at 0.5 [0.75] m/E.

are based upon a maximum rate of 10^8 photons/s on target and 400 MHz per GeV in the tagger.

The linear polarization of the photons in the coherent peak is shown in Fig. 4.4 as a function of the energy of the electron beam. This figure demonstrates why it is essential to have electrons of as high energy as possible, even though photon energies of no more than 9 GeV are required. The intensity of the coherent peak, not shown in the figure, has a similar dependence on the electron beam energy in this region.

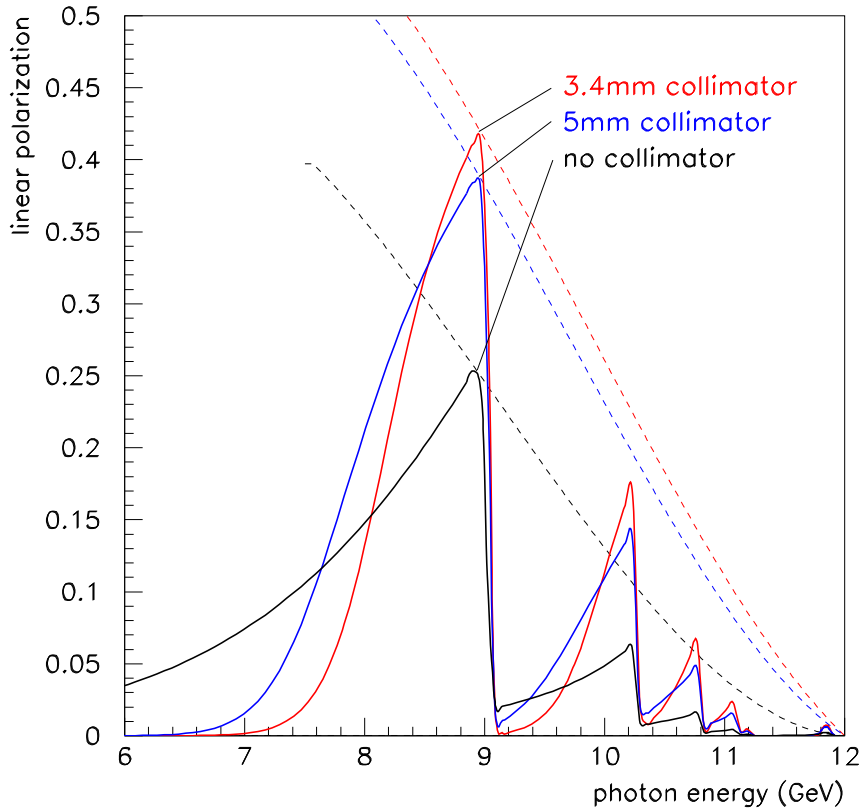

Figure 4.5: Linear polarization of the coherent bremsstrahlung beam for a fixed electron beam energy of 12 GeV. The dashed lines indicate the trajectory of the peak polarization as the peak energy is swept by rotating the crystal. The 3.4 mm [5 mm] collimator represents a cut at 0.5 [0.75] m/E.

Shown in Fig. 4.5 is the linear polarization of the photon beam *vs* photon energy for fixed electron beam energy. The dashed curves show how the maximum polarization in the primary peak varies as the peak energy is changed by rotating the crystal. The polarization in all cases is zero at the end-point. Without collimation it rises as $(E_0 - k)^2$, one power coming from the intensity of the coherent peak relative to the incoherent component, and the other from the intrinsic polarization of the coherent photons. Collimation allows one to essentially isolate the coherent component, so that the polarization available to the experiment rises from zero at the end-point in a linear fashion. The dashed curves in Fig. 4.5 demonstrate this point.

In order to obtain the full polarization enhancement from collimation, it is necessary to have a distance between the radiator and collimator on the order of 100 m. This distance scale is set by the requirement that the collimator aperture must be large compared to the virtual electron beam spot on the collimator but small compared to the actual photon spot size. The virtual electron beam spot is defined as the profile that the electron beam would have at the entrance to the collimator if it were allowed to propagate freely instead of being bent by the tagger dipole field into the beam dump.

The size of the virtual spot at the collimator is determined by the beam emittance combined with an upper limit of 20 μr on the angular spread of the electron beam at the radiator. The latter value was chosen to match the spread in the beam incidence angle to the mosaic spread of the crystal because it is the combination of the two that limits the definition of the coherent edge. Taking a conservative estimate of 10^{-8}m·r for the 12 GeV electron beam emittance[3] leads to a virtual spot size of 0.5 mm r.m.s. (1.2 mm f.w.h.m.). Note that this argument does not assume any scale for the radiator-collimator distance. The size of the real photon spot is given by one characteristic angle m/E which defines a circle on the collimator containing approximately 50% of the total photon intensity. The real spot size is proportional to the radiator-collimator distance. At a distance of 75 m the ratio of spot sizes is 6, sufficient to allow collimator apertures that satisfy both of the above inequalities.

Fig. 4.6 shows the peak polarization of the beam as a function of radiator-collimator distance for a coherent peak at 9 GeV. In this calculation the collimator diameter is held constant at 3.4 mm to make sure that the virtual beam spot of 1.2 mm f.w.h.m. is well-contained within the aperture, which is the main condition for effective collimation. At zero distance the collimator has no effect except to attenuate the beam, and so the uncollimated polarization

[3]Simulations of the 12 GeV accelerator design indicate that the horizontal emittance of the beam will be a factor 2 better than this, and a factor 4 bette in the vertical.

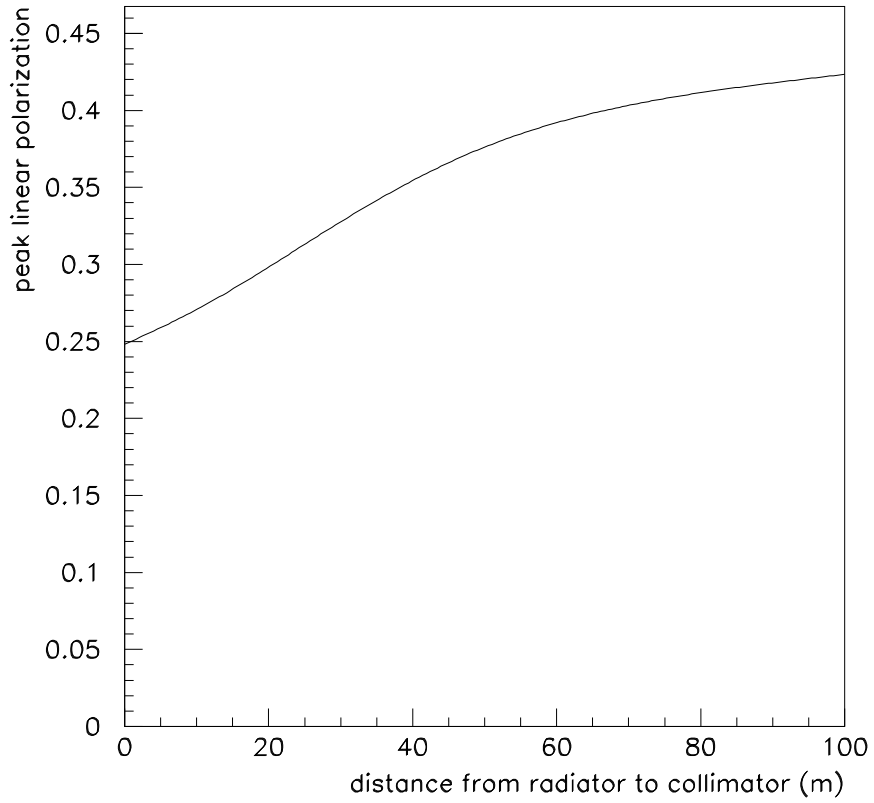

Figure 4.6: Maximum polarization *vs* radiator-collimator distance for a coherent peak at 9 GeV. The collimator diameter is held fixed in this calculation to keep a constant ratio between the sizes of the virtual electron spot and the collimator.

from coherent bremsstrahlung is obtained. At 100 m separation distance the polarization enhancement from collimation has saturated. The design for Hall D calls for a radiator-collimator distance of 75 m.

crystal	best reciprocal vector	$P/P_{diamond}$
diamond	2,-2,0	1.00
beryllium	0,0,2	0.86
boron	2,0,8	0.38
silicon	2,-2,0	0.19
Be_2C	2,2,0	1.10

Table 4.1: Figure of merit for various materials that might be used as a coherent bremsstrahlung radiator. This table is reproduced from Table 2 in Ref. [2].

4.3 Choice of radiator

The ideal radiator would be a layered structure with strong transverse fields that alternate between layers spaced about 50 nm apart, thus simulating the standing wave in a cavity driven by a 15 eV laser. While it is possible to construct ordered materials with unit cells as large as this, the self-shielding of atoms means that beyond the atomic length scale the residual fields are comparatively weak. Hence heterogeneous structures are not viable for use as a coherent radiator. Since the strong fields inside a solid are revealed at the atomic scale, the first requirement for a good radiator is that the unit cell be compact and closely packed. The best radiators are those with the smallest unit cells because these provide the best match between the atomic and the crystal form factors. This match is best for the light elements, and essentially prohibits the effectiveness of materials containing substantial amounts of any elements heavier than carbon. An extensive survey of possible radiator materials is presented in Ref. [2]. In Table 4.1 is shown the figure of merit that those authors report for favored crystalline materials. The figure of merit is the product of the atomic times the crystal form factor evaluated at the leading peak, normalized to the value for diamond.

Table 4.1 shows that the list of viable materials for a crystal radiator is relatively short. Silicon would be an excellent choice from the point of view of price and fabrication, but unfortunately it is far inferior in terms of performance. The material shown with the highest figure of merit is the binary crystal Be_2C. In general, multi-element crystals are more sensitive to radiation damage than single-element crystals because annealing of dislocations is significantly less efficient when more than one atomic species is involved. This leaves diamond and beryllium as the two alternatives.

Both diamond and beryllium have unusually high Debye temperatures. A high Debye temperature is important for a bremsstrahlung radiator material for three reasons. First, the cross section for coherent bremsstrahlung from a discrete crystal momentum vector $\vec{q}$ contains a factor $e^{-q^2/4M\theta_D}$ which reflects the fact that position fluctuations of atoms in the lattice diminish the coherent effect. This factor is near unity for the low-order crystal momenta provided that the Debye temperature θ_D is sufficiently large. Second, the Debye temperature is, roughly speaking, a measure of the stability of the crystal structure and hence its capacity to survive significant doses of radiation. Third, the radiator material will inevitably be heated by the beam, and will normally operate in vacuum well above the ambient temperature. A high Debye temperature means that there is a large range of temperatures over which the material may operate without degraded performance as a crystal radiator. The Debye temperature of diamond is 2200°K, while that of beryllium is 1400°K.

Considerable experience exists with both diamond and beryllium single crystals for use as monochromators within in the X-ray diffraction community. Single crystals of both can be produced with diameters larger than 10 mm, which is sufficiently large for use as a coherent bremsstrahlung radiator. However there are a number of features, besides the performance figure showin in Table 4.1, that make diamond a clear winner in this application. First of all, diamond has a thermal conductivity that is a factor 10 larger than that of beryllium. Although both are excellent thermal conductors, the difference makes a difference when the crystal is made very thin, while keeping the heat load constant, which is the optimization scenario for a coherent bremsstrahlung source. As shown in a following section, the thermal load on the radiator in the Hall D source is enough to heat the crystal to several hundred degrees at full operating intensity. Therefore a factor 10 higher thermal conductivity is a significant advantage for diamond. Combined with this, the thermal expansion coefficient for beryllium is about a factor 10 higher than that of diamond, which means that it will be much more subject to thermal stress and distortion in the beam than will diamond. More importantly, published rocking curves for beryllium single crystals have widths greater than 300 μr f.w.h.m., as compared with less than 20 μr f.w.h.m. for the best large-area diamonds [5]. For these reasons, diamond has been adopted as the unique choice for the radiator material in the Hall D coherent bremsstrahlung source.

Most of the experience to date with coherent bremsstrahlung has been with diamond radiators. Extensive expertise with large diamond crystals, such as would be required for the production of coherent bremsstrahlung radiators, already exists within the gem industry [6, 7]. Although the details of the crystal growth process are typically treated in the highly competitive diamond

business as sensitive corporate information, researchers both in Europe and Japan have been able to obtain large-area crystals from the firms Element Six and Sumitomo Electric Industries and demonstrate that they have X-ray rocking curves that are very close to the theoretical ideal for a perfect crystal [8, 9]. Within the GlueX collaboration, the University of Glasgow group has been able to obtain a significant number of high-quality crystals from Element Six, cut along the desired crystal direction and polished down to a desired thickness. The techniques used for assessing the quality of the diamonds are discussed in the next section.

In general terms, diamonds are classified as type I or type II, where type II have been subjected to greater stresses during their formation than type I. Commonly, type II exhibit substantial plastic deformation. Diamonds are also classified according to the form in which nitrogen atoms are present in the crystal lattice. In type *a* the nitrogen is aggregated into clusters of atoms, whereas in type *b* the nitrogen is almost uniformly distributed throughout the crystal. For coherent bremsstrahlung radiators, type Ib diamonds are the most suitable. Unfortunately, type Ib natural diamonds are very rare. The only known way to obtain large high-quality Ib diamonds is through the process of synthetic crystal growth. The primary impurity in these synthetics is nitrogen, which is artificially introduced as a growth catalyst. At present type Ib diamond mono-crystals can be obtained with nitrogen concentrations as low as 100 ppm.

Synthetic diamonds are made using either vapor deposition (CVD) or high pressure high temperature (HPHT) techniques. CVD diamonds have an extensive mosaic and are unsuitable for coherent bremsstrahlung. Synthetics from the HPHT process are not uniform in their crystal quality, but it is not rare to find large regions of a crystal that approach the theoretical limit in the X-ray rocking curve width. Among the high-quality crystals obtained by the Glasgow group from Element Six, one of them was polished down to a thickness less than 18 microns, demonstrating the feasibility of producing the 20 micron diamonds needed for GlueX.

4.4 Crystal quality

In the calculation of the coherent bremsstrahlung spectrum it is necessary to take into account the fact that even the very best crystals have some dislocations and other defects. Besides locally disrupting the regularity of the crystal, these defects impose stresses which produce small ripples in the crystal planes. If these ripples were amplified, the surface of a crystal would appear like a mo-

saic of planar regions whose local normal unit vectors are slightly misaligned with one another. The angular scale of the deviations between the local normals across the face of a single crystal plane is termed the *mosaic spread* of the crystal. Because crystal lattice distortions affect all of the planes in that region of the crystal, mosaic spread tends to have the same scale for all sets of planes in a given region, and is characterized by a single parameter. In coherent bremsstrahlung, the mosaic spread contributes in the same way as electron beam divergence to the blurring of the exact energy-angle relation for coherent photons.

Besides dislocations, there are other kinds of crystal defects. The presence of foreign atomic species during the crystal growth process can result in the substitution of impurities at some lattice sites, or the formation of voids where impurities tend to collect in clusters of several atoms. In the growth of diamond crystals under conditions of high pressure and temperature, the growth rate is greatly enhanced by the presence of a small amount of nitrogen. Thus it is normal that small amounts of nitrogen impurities should exist even in the best natural stones, as well as in the synthetics created by the HPHT process.

The ideal conditions for growth of a perfect synthetic crystal require pre-existing mono-crystalline diamond with clean planar facets cleaved along the major crystal planes, upon which new layers of carbon are deposited in succession. If conditions are right, the registry of the atoms with the original crystal is preserved over millions of deposited layers, starting from the original seed. In principle, the new planes of the regular lattice should continue to match up perfectly at the boundaries between the different growth surfaces that originated on the facets of the seed, but in practice the strains from the accummulation of small imperfections that occur during the growth process tend to build up there, forming recognizable patterns of concentrated defects known as *growth boundaries*. If the stresses grow too large then new strain regions develop, leading to a more pronounced mosaic pattern in the subsequent layers.

Unfortunately the growth process has proved difficult to control in a reproducible fashion. As a result, out of several dozen stones produced, typically only one or two are of sufficient quality for use as a coherent bremsstrahlung radiator for. The selection process described below was formerly developed by the Glasgow group to supply crystals for the coherent bremsstrahlung source at Mainz, Germany and subsequently for the Hall B source at Jefferson Lab. The requirements for Hall D are very similar to those of Mainz and Hall B, except that the electron beam current will be higher by about an order of magnitude and the crystals will be thinner.

To produce a coherent bremsstrahlung radiator from a synthetic diamond,

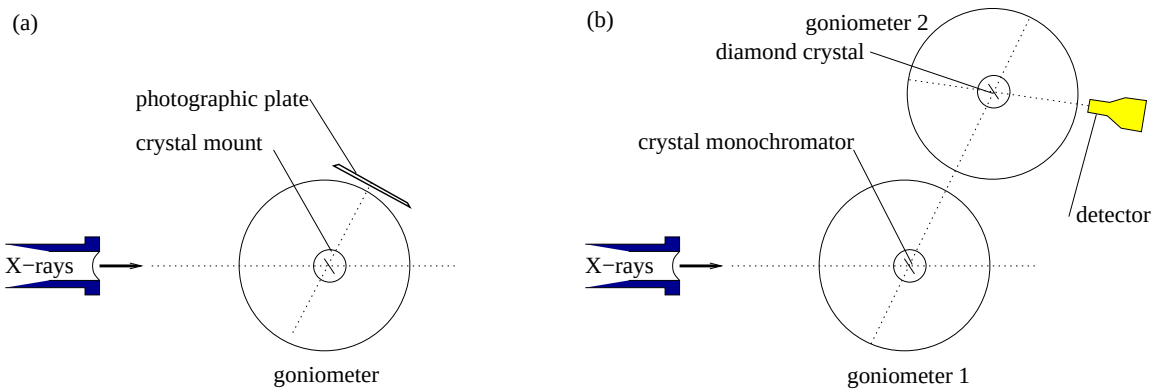

Figure 4.7: Experimental setup for assessment of diamond crystals at the Daresbury Synchrotron Light Source beam line, configured for topograph measurements (a), and rocking curves (b).

the ingot from the synthetic process was sliced into sections along the (1,0,0) axis using a diamond saw. This cut was made by the vendor at the laboratory where they are produced. Sample slices from different regions along the axis were provided to the Glasgow group for assessment. The samples were first examined under a microscope with polarized light. Crystals which exhibit large plastic deformation were discovered and eliminated at this stage. Those which appeared clear and featureless under polarized light where then taken to a synchrotron light source and examined using X-ray diffraction. Two types of X-ray measurements were performed, topographs and rocking curves.

1. Topographs
   A topograph is a real-space image of a diamond formed from X-rays that Bragg-scatter from a particular set of planes in the crystal, as shown in Fig. 4.7a. Using the highly-parallel X-ray beam from the Daresbury Synchrotron Light Source (SRS) and setting the detector at twice the Bragg angle for a known set of planes for diamond, X-rays of the appropriate wavelength to satisfy the Bragg condition are scattered at a precise angle θ into the detector. If the crystal is a single crystal then the X-ray image formed on the plane of the detector is a real-space image of the crystal, called a *projection topograph*. If the vertical slits defining the X-ray beam are narrowed forming the incident beam into a thin ribbon a few μm wide, then the image at the detector reveals a slice though the crystal, called a *section topograph*. Projection topographs reveal any large-scale imperfections in the crystal. Section topographs

can be used to examine the depth profile of imperfections. Topographs sample the whole volume of the crystal. Hence, by measuring projection and section topographs, a 3-dimensional picture of the diamond can be obtained. It is also possible to differentiate between screw and edge dislocations. The topograph image reveals dislocations, growth boundaries and any feature which suppresses or enhances Bragg scattering at the selected angle. In principle, topographs taken at different angles provide independent views of the crystal structure. In in practice, however, the imperfections that are revealed with one set of planes appear in a similar fashion when viewed from other orientations.

2. Rocking curves
   A rocking curve is a plot of Bragg-scattering intensity *vs* angle between the incident X-ray beam and the normal to the crystal planes. A diagram of the setup used at the Daresbury SRS is shown in Fig. 4.7b. First the broad-band X-ray beam from the SRS is monochromated by scattering at a known fixed angle from a reference crystal, in this case silicon. This beam is then directed at the diamond crystal under study, from which it scatters a second time and is detected. The scattering is appreciable only when the diamond is at just the right angle with respect to the incident beam such that the Bragg condition is satisfied at both crystals. The variation in the scattering intensity with angle as the diamond wafer is rotated through the scattering peak is called the *rocking curve* for that diamond. A perfect crystal exhibits a rocking curve consisting of a single peak whose width is called the *natural width* and depends on the material and the crystal plane. The natural width of the (2,2,0) planes in diamond is about 5 μr. Instead of a single peak, for actual crystals one typically sees a number of peaks spread out over a region in angle known as the rocking curve width. Rocking curves widths, for a selected set of crystal planes, measure quantitatively how defects distort the crystal lattice. By adjusting the slits it was possible to examine the rocking curve in a local region of the crystal or to measure the entire crystal at once. From the rocking curves it is straight forward to determine how close to ideal the lattice structure of the diamond is for coherent bremsstrahlung.

Figs. 4.8-4.9 show some of the results that were obtained at the SRS in January, 2002. At the left of the figures is shown a projection topograph taken with the (0,4,0) planes. At the right is shown the corresponding rocking curve taken in combination with a silicon crystal set to reflect from the (3,3,3) planes at a wavelength of 1Å. The two diamond wafers had been cut from the

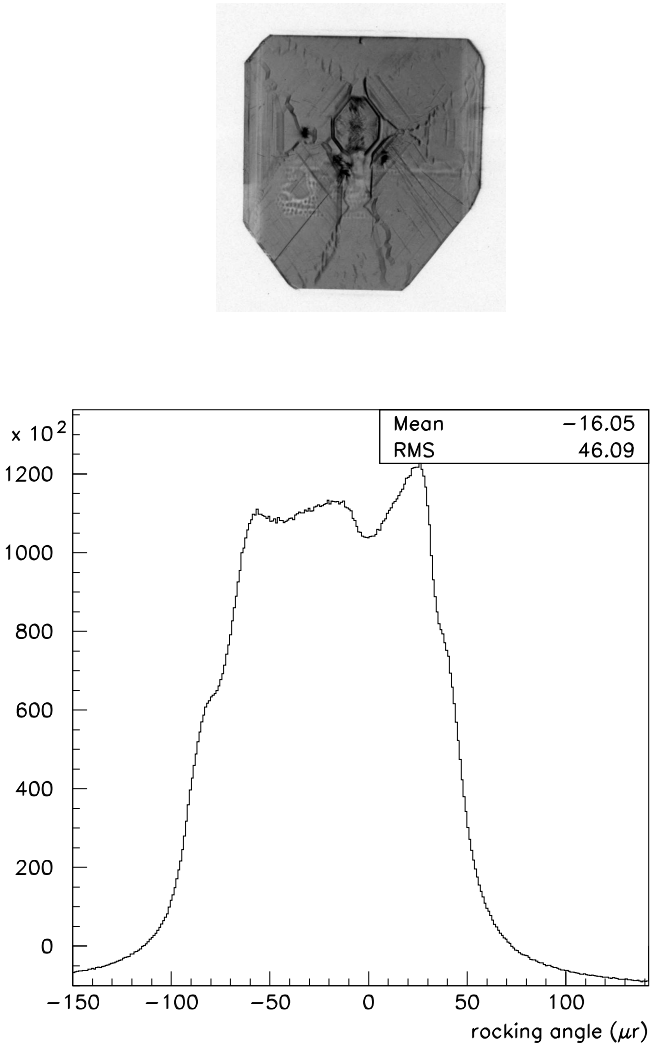

Figure 4.8: Experimental data collected using highly-parallel X-rays from the Daresbury SRS light source for stone 1482A slice 3 (close to the seed). At the top is shown a projection topograph of the wafer taken using the broad-band X-ray beam and a Polaroid film placed at the angle for reflection from the (0,4,0) planes. The image is a magnified by a factor of 5. The graph shows the rocking curve for the same set of planes, taken using a NaI counter and 1Å X-rays monochromated by a silicon crystal.

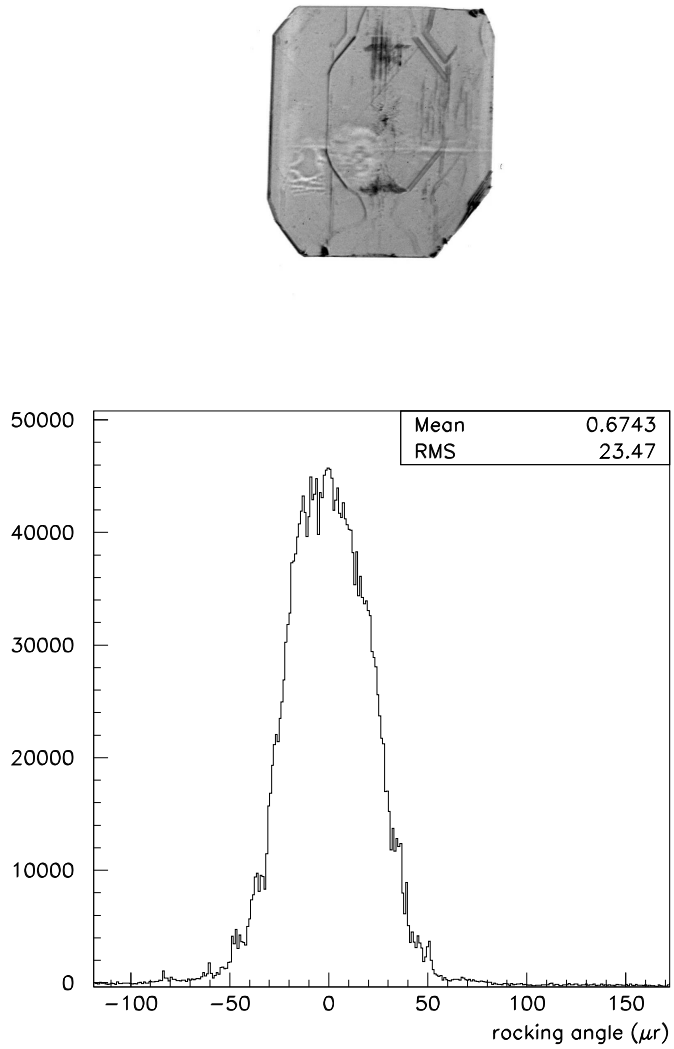

Figure 4.9: Experimental data collected using highly-parallel X-rays from the Daresbury SRS light source for stone 1482A slice 2 (further from the seed). At the top is shown a projection topograph of the wafer taken using the broad-band X-ray beam and a Polaroid film placed at the angle for reflection from the (0,4,0) planes. The image is magnified by a factor of 5. The graph shows the the rocking curve for the same set of planes, taken using a NaI counter and 1Å X-rays monochromated by a silicon crystal.

same original type Ib stone, with Fig. 4.8 coming from the end close to the seed, and Fig. 4.9 coming from near the middle of the ingot. The topographs are negatives, meaning that the image is dark in regions where the X-ray intensity was largest.

The first thing to notice from the topographs is that both wafers are monocrystalline; there are no regions within the boundaries of the crystal where X-rays do not scatter. Even so, there are important differences between the two samples. The growth boundaries (the picture-frame pattern) which are visible in Fig. 4.8 spread out and become less pronounced in slice 2 which was taken further from the seed. It is interesting that the strain pattern appears mostly as dark regions rather than light, which indicates stronger scattering in the defects than in the ordered regions. This is expected because the crystal is thick enough to scatter essentially 100% of the beam photons that fall within the peak region in the rocking curve, so the wider is the rocking curve, the wider the energy bite of the broad-band beam that is scattered. It should be recalled that both crystals appeared clear and featureless under polarized light at visible wavelengths. Only X-rays can reveal the significant defect structure of these crystals.

The specification for a diamond radiator for use as a coherent bremsstrahlung radiator in Hall D is that the rocking curve width be no greater than 20 μr r.m.s. The conclusion drawn from the rocking curve measurements is that slice 2 is a good candidate for use in the GlueX experiment, and that slice 3 is not. Having confirmed the quality of slice 2, it would have been possible to request that the manufacturer cut several wafers from the same region of the original stone, and expect that the quality of the new slices will be similar. This was not done because at that time the demand for new crystals was one or two every few years. In the case of Hall D it will be important to take advantage of such efficiencies in order to obtain a steady supply of new radiators to replace those damaged by radiation.

4.5 Crystal thickness

The range of permissible thicknesses for a crystal radiator is bounded both from above and below. It is bounded from above by multiple scattering of the electron beam as it passes through the radiator, which causes the divergence of the incident beam to grow, thereby enlarging the photon beam spot on the collimator face and degrading the degree to which collimation discriminates against the incoherent component in favor of the coherent part. It is bounded from below by the rate of radiation damage that increases for thinner crys-

tals, as the electron beam current is increased to maintain the desired beam intensity.

There is a second and more fundamental lower bound imposed by the fact that the crystal must have some minimum thickness in order to achieve the full coherent gain. The calculation of the coherent bremsstrahlung cross section begins with the assumption of an infinite crystal, but practically this means only that the crystal is large compared to some characteristic scale. It is important to identify what the characteristic scale is in this problem in order to know how thin one can make the crystal without hurting performance. In the analogous case of the Mössbauer effect, one can estimate the number of atoms participating in the collective absorption by looking at the emission time of the photon (lifetime of the radiating transition) and asking how many nuclei lie within the envelope of the photon wave packet. In the coherent bremsstrahlung process, the lifetime of the radiating system is given in the lab system by the uncertainty principle and by how far the electron energy deviates from its on-shell value between absorbing the virtual photon and emitting the real one. The latter quantity is almost exactly given by q_z , the initial-state virtual photon momentum component along the incident electron axis. This means that the electron travels an average distance $\lambda = \hbar c/q_z$ during the interaction. For a given coherent peak at normalized energy x in the photon spectrum, the coherence length is given by

$$\lambda = \frac{2\hbar E(1-x)}{xm^2c} \tag{4.3}$$

From this simple argument one sees that the coherent gain goes linearly to zero at the end-point, a result that is borne out by the full QED calculation. One also sees that the lower limit on crystal thickness imposed by the coherence length depends upon both the electron beam energy and the photon energy. For 12 GeV electron beam energy and a 9 GeV coherent photon the coherence length is 6 nm, or about 17 unit cells for diamond. This shows that the coherence length does not impose a practical limit on how thin the radiator should be for GlueX.

The effects of multiple scattering are best presented by showing the calculated spectra for various radiator thicknesses. In Fig. 4.10 is shown the photon spectrum for diamond radiators of thickness 10, 20, 50, and 100 microns. The electron beam current in each case is rescaled to keep the rates in the tagger constant. The loss in normalized intensity with the thicker radiator and as the broadening of the left edge of the peak are due to the smearing out of the photon beam spot on the collimator face due to multiple scattering of the electron beam in the crystal prior to radiation. The plot shows that improvements in

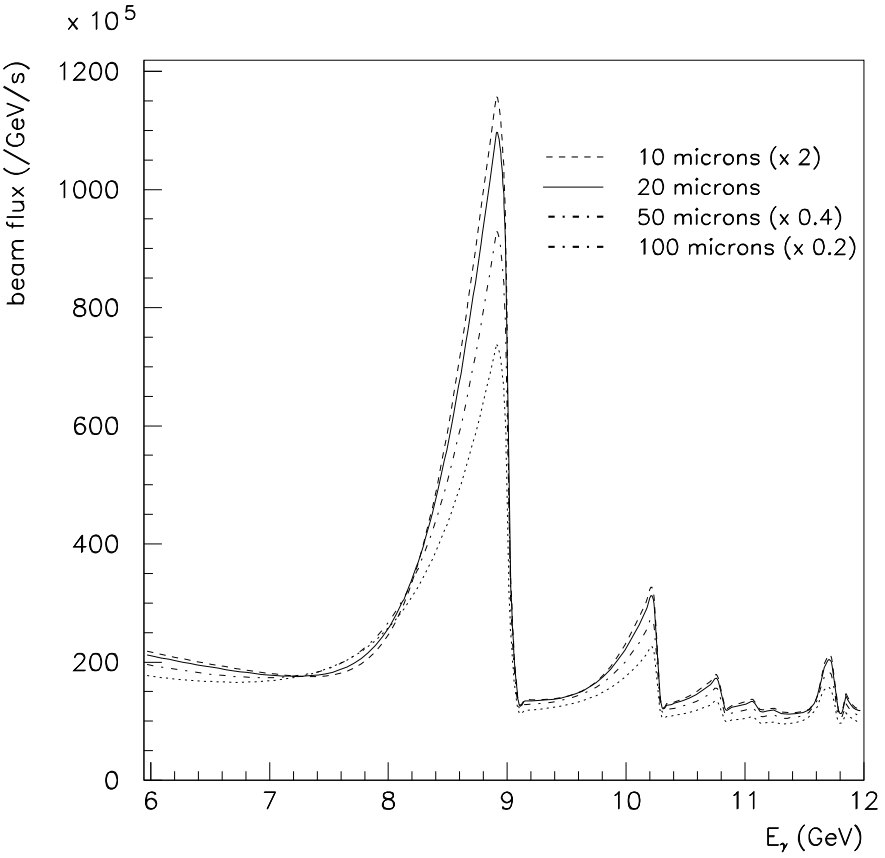

Figure 4.10: Collimated coherent bremsstrahlung spectrum from a 12 GeV electron beam using diamond radiators of different thicknesses. The beam currents have been renormalized to keep the rates in the tagger constant. The calculation assumes a 3.4 mm collimator located 75 m from the radiator, and standard values for beam emittance and crystal mosaic spread.

Axis	Motion	Range	Step size
x	horizontal translation	-50 mm – +50 mm	0.01 mm
y	vertical translation	-20 mm – +20 mm	0.01 mm
θ_v	vertical rotation	-100 mr – +100 mr	10 μr
θ_h	horizontal rotation	-100 mr – +100 mr	10 μr
ϕ	azimuthal rotation	-100° – +100°	0.01°

Table 4.2: Requirements for goniometer axes

the coherent / incoherent flux ratio with decreasing radiator thickness saturate around 20 microns. The design for the GlueX photon source specifies diamond radiators of thickness 20 microns.

4.6 Crystal mount

It has already been shown that in order to achieve appreciable coherent gain the crystal must be oriented so that the coherent peaks appear well below the end point. Eq. 4.2 shows that this condition is equivalent to requiring that the dot product of the crystal momentum vector corresponding to the coherent peak and the beam momentum vector be of order m^2. For $p = 12$ GeV/c and $q \sim 10$ keV, this amounts to requiring that p and q be mutually perpendicular to within about a degree, and within one degree of variation the coherent peak sweeps out nearly the full range in x from 0 to 1.

Hence, to have a stable photon beam with the coherent peak positioned at the right energy, the angle between the incident electron beam and the crystal radiator must be adjustable in steps of a few μr and remain stable at this level. Since the angle of the incident beam is fixed by the beamline optics and the position of the photon collimator, incidence angle adjustments are made by changing the orientation of the crystal. This is achieved with a precision goniometer (shown schematically in Fig. 4.11). A goniometer with three rotation axes and two translation axes gives the necessary control over both where the beam spot is located on the crystal and what its angle is with respect to the beam direction. Rotation about the azimuthal axis ϕ sets the orientation of the polarization plane. Rotations about the θ_v, θ_h axes select the energy of the coherent peak and provides an additional handle for eliminating extra peaks in the spectrum from unwanted lattice vectors. Estimates of the approximate range and step size for each of the axes are given in Table 4.2.

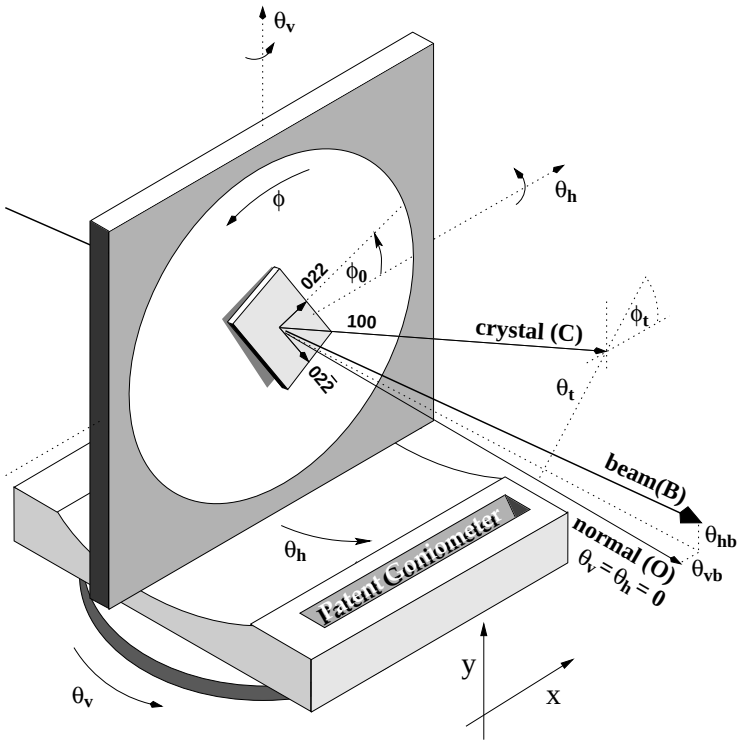

Figure 4.11: Schematic illustration of crystal mounted in goniometer

It is foreseen that the crystal goniometer will hold a target ladder in which several targets are mounted, which can be interchanged under remote control. The minimum requirement for the ladder is a diamond crystal, an amorphous radiator, a blank position, and a fluorescent screen to show the position and shape of the beam spot. A second diamond radiator would also be useful, in case the first one is damaged in some way. A goniometer with the required precision can be obtained commercially. Remote control of all stages of the goniometer is a part of the slow controls plan for the GlueX experiment.

4.7 Crystal alignment and monitoring

As can be seen in Fig. 4.11 the goniometer setting θ_v,θ_h defines the direction of the vector normal to its inner plate (O). Ideally, at its zero setting $\theta_v = \theta_h = 0$ this normal vector would coincide with the electron beam direction (B), but in practice there are small offsets θ_{vb}, θ_{hb} which vary slightly with the tune of the electron beam. There are also two other corresponding offsets that specify the direction of the (1,0,0) axis of the crystal with respect to the inner plate normal vector. These arise both from imperfections in the way that the crystal is mounted in its holder, and from imperfections in the way that the crystal was originally cut. These corrections can be parameterized in terms of the tilt θ_t of the (1,0,0) crystal axis from the O direction, and also its azimuthal vector ϕ_t. A third offset angle ϕ_0 is also needed to specify the azimuthal plane containing the (0,2,2) axis direction in the coordinate system of the goniometer mount. Once the goniometer θ_v and θ_h have been adjusted to align the (1,0,0) crystal axis with the beam direction B then the (0,2,2) direction is normal to the beam and the gonimeter azimuthal setting ϕ - ϕ_0 determines the plane of polarization of the beam relative to the horizontal.

Each time a new crystal is installed, the offsets θ_{v0}, θ_{h0}, and ϕ_0 must be determined empirically by systematically rotating the crystal while monitoring the positions of the coherent peaks in the coherent bremsstrahlung spectrum seen in the rates measured by the tagger focal plane counters. A collimated photon spectrum is not required for the alignment procedure, but it is essential to sample low enough in the photon energy spectrum to see the peaks at low x. For this reason, the tagger focal plane is instrumented with a broad-band counter array that covers the full energy spectrum from 3 GeV up to 11.7 GeV. Simply counting the singles rates in the broad-band array with scalers and plotting them in a two-dimensional histogram versus the wobble angle of the crystal provides the fast feedback that allows the alignment procedure to be completed in a relatively short period of time. During normal running after

the alignment has been carried out, the broad-band tagging counters provide essential online diagnostics to monitor drifts in angles caused by changes in the beam tune, thermal effects in the crystal mount, and radiation damage. If necessary a feedback system could be implemented via the slow control system, where any drift in the position of the coherent peak could be corrected by periodically adjusting the goniometer angles within predefined limits.

4.8 Crystal lifetime

There are no published results that give precise information about the kinds and densities of crystal defects in diamond as a function of dose. The best estimates for crystal lifetime in a coherent bremsstrahlung source are found in an unpublished SLAC report [10] which states that "serious degradation" of the coherent bremsstrahlung spectrum was observed after 2-5 Coulombs of electrons had passed through the crystal. The SLAC beam energy was 19.7 GeV, which should not be much different from 12 GeV for these purposes. The SLAC beam spot was large enough to fill the entire crystal, of approximate area 1 cm^2, although this is not to say that the beam intensity was uniform over that area. From these results can be derived a useful upper bound of about 0.25 Coulomb/mm^2 on the integrated current that can pass through a diamond before it must be replaced. In the same report claims are made that it was possible to recover acceptable performance from a damaged diamond by annealing it in a high-temperature oven. The annealing procedure was found to work over several use cycles, before the accumulated damage was so severe that the diamond could no longer be used.

The best quantitative information on crystal degradation from radiation damage comes from X-ray studies performed by the Glasgow group of a diamond which had been used in the MAMI coherent bremsstrahlung source at Mainz for several years[8]. The electron beam on the Mainz crystal had a full width of about 100 microns. It was estimated that 5-10 Coulombs of electrons had passed through the diamond during its use in the source. There was a small greenish black spot visible where the beam had passed through the diamond. This small beam spot means that the exposed region of this crystal had seen three orders of magnitude more integrated charge than allowed by the upper limit estimated above based on the experience reported by the SLAC group. Indeed, X-ray rocking curve measurements with a very small X-ray beam showed that in the center of the beam spot the rocking curve was split into many peaks, and that the full width was several mr. However 2 mm away from the damage center, a single narrow peak was seen in the rocking curve,

with essentially the same width as had been observed for the pristine crystal. This confirms that the lifetime of a crystal can be extended by occasionally moving the beam spot on the face of the crystal.

The area of the beam spot on the damaged MAMI radiator is two orders of magnitude smaller than what is being planned for Hall D. A larger spot means a longer crystal lifetime before radiation damage substantially degrades the crystal properties. Appropriately scaled, the exposure of the Mainz crystal in the center of the beam spot corresponds to more than 10 years of running in Hall D at full intensity without a spot move. Plans for the Hall D source are to keep the local dose three orders of magnitude less than this. Based on the estimated upper limit stated above, the Hall D source can run at a full intensity of 2 μA for 100 hours before it is necessary to move the spot on the crystal. If it had no bad zones, a square crystal of area 5×5 mm^2 would accommodate 5 spot moves before the crystal would need to be replaced.

Measurements of crystal radiation damage rates will be made during the first two years of GlueX running. During those two years, the source will operate at 10% of design intensity, permitting a single crystal to last for an entire year of running. These same estimates suggest that as many as 5 diamonds per year will be required to run the Hall D source at full intensity. It may or may not turn out to be economically advantageous to try annealing damaged crystals, depending on the availability and cost of new diamonds at that time.

Another issue related to crystal degradation is that of heat dissipation for very thin crystals. The heat from the ionization energy loss of the beam as it passes through the crystal must be dissipated either via conduction through the crystal mount or via thermal radiation. Although the ionization energy loss is small compared to that from bremsstrahlung, it is not entirely negligible at beam currents planned for Hall D. It can be calculated using the restricted energy loss formula, which yields 21 mW for a 20 micron crystal at a current of 2.1 μA. This is not much power, but the crystal is very thin. Diamond has a very high melting point; at low pressures it sublimates at about 4027°C. However it begins to transform into graphite above 707°C, at a rate that increase with temperature. It is essential that the crystal at the center of the beam spot stay well below this limit.

The diffusion equation including a heating term and one for radiative cooling can be written as

$$C_P\, a\, \frac{dT}{dt} = h(x,y) - 2\sigma\left(T^4 - T_0^4\right) + \kappa\, a \nabla^2 T$$

where the heating term $h(x,y)$ has units of power/area, σ is the Stefan-

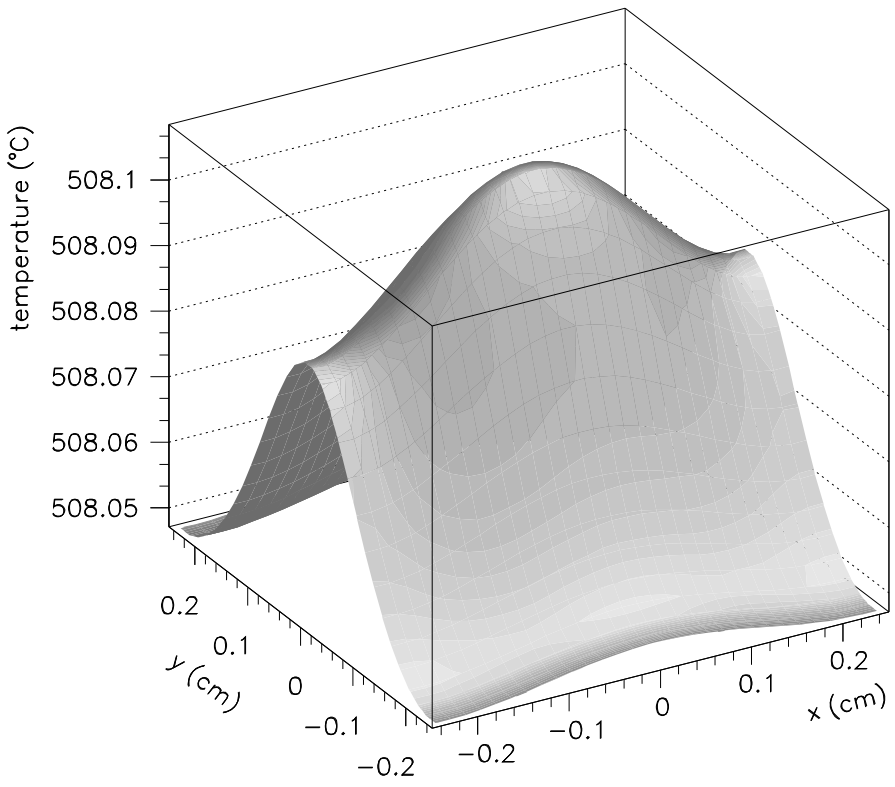

Figure 4.12: Calculated temperature profile of diamond crystal with a 12 GeV beam at the maximum electron beam current of 2 μA. The crystal dimensions are 5 mm $\times$ 5 mm $\times$ 20 microns. The ambient room temperature was taken to be 27°C (300°K). The azimuthal asymmetry is caused by the elliptical shape of the electron beam spot on the radiator.

Boltzmann constant, C_P is the heat capacity and κ the coefficient of conduction for diamond, and a is the thickness of the crystal. T_0 is the ambient temperature of the environment and T is the local crystal temperature, a function of space and time coordinates. After a certain time, T converges to the steady-state solution shown in Fig. 4.12. The calculation used a crystal of dimensions 5 mm $\times$ 5 mm $\times$ 20 microns and a beam current of 2 μA. This calculation shows that the conductivity of diamond is sufficient to prevent significant temperature gradients across the crystal even for very thin wafers. It also shows that radiative cooling alone is sufficient to dissipate the heat being generated by the beam passing through the crystal and keep the entire crystal well below the graphite transition temperature. This calculation includes only radiative cooling, and shows that the crystal mount does not need to be designed to dissipate heat from the crystal. It does indicate, however, that the materials used to attach the diamond the mount must either be capable of maintaining their mechanical properties at 500°C or be sufficiently thermally conductive themselves to allow 20 mW of heat to be removed from the diamond by conduction to the mount.

List of Figures

List of Tables

Bibliography

[1] W. Kaune, G. Miller, W. Oliver, R.W. Williams, and K.K. Young. Inclusive cross sections for pion and proton production by photons using collimated coherent bremsstrahlung. *Phys. Rev.*, D**11**(3):478–494, 1975.

[2] H. Bilokon, G. Bologna, F. Celani, B. D'Ettorre Piazzoli, R. Falcioni, G. Mannocchi, and P. Picchi. Coherent bremsstrahlung in crystals as a tool for producing high energy photon beams to be used in photoproduction experiments at CERN SPS. *Nuclear Inst. and Meth.*, **204**:299–310, 1983.

[3] G. Diambrini-Palazzi. *Revs. Mod. Phys.*, **40**:611, 1968.

[4] U. Timm. *Fortschr. Phys.*, **17**:765, 1969.

[5] F. Mucklich and G. Petzow. Development of beryllium single crystal material for monochromator applications. *Mineral Processing and Extractive Metalurgy Review*, 13:193, 1994.

[6] S.L. Clewes, N. Perkins, M.L. Markham, H.K. Dhillon, I. Friel, D.J. Twitchen, and representing Element Six LTD G.A. Scarsbrook. Synthetic single crystal diamond: State of the art. In *Diamond, Diamond-like Materials, Carbon Nanotubes, and Nitrides* [11]. 19th European Conference on Diamond, Diamond-like Materials, Carbon Nanotubes, and Nitrides, Sitges, Spain, Sept. 7-11 2008.

[7] A. Ueda, Y. Akahane, Y. Nishibayashi, and LTD. T. Imai, representing Sumitomo Electric Industries. Development and evaluation of a diamond electron source for electron beam instruments. In *Diamond, Diamond-like Materials, Carbon Nanotubes, and Nitrides* [11]. 19th European Conference on Diamond, Diamond-like Materials, Carbon Nanotubes, and Nitrides, Sitges, Spain, Sept. 7-11 2008.

[8] J.D. Kellie, P.J.M. Clive, G.L. Yang, R. Beck, B.C. Evans, C. Gordon, C. Hall, J.W. Harris, R.T. Jones, D. Laundy, K. Livingston, I.J.D. MacGregor, J.C. McGeorge, J. Malone, A. Schmidt, P.A. Slaven, R.M. Vrcelj, and D. Watts. The selection and performance of diamond radiators used in coherent bremsstrahlung experiments. *Nuclear Inst. and Meth.*, A**545**:164, 2005.

[9] K. Tamasaku, T. Ueda, D. Miwa, and Tetsuya Ishikawa. Goniometric and topographic characterization of synthetic iia diamonds. *J. Phys. D: Appl. Phys.*, **38**:A61, 2005.

[10] R. Schwitters. The slac coherent bremsstrahlung facility. *SLAC technical note*, SLAC-TN-70-32, 1970. (unpublished).

[11] Diamond and Related Materials, 2008. 19th European Conference on Diamond, Diamond-like Materials, Carbon Nanotubes, and Nitrides, Sitges, Spain, Sept. 7-11 2008.